Contents lists available at ScienceDirect

Applied Catalysis B: Environmental

Research paper

Chemical-bond conjugated BiO(OH)$_x$I$_{1-x}$-AgI heterojunction with high visible light activity and stability in degradation of pollutants

Huanhuan Ji [a,b], Lili Zhang [a], Chun Hu [a,b,c,*]

[a] Key Laboratory of Drinking Water Science and Technology, Research Center for Eco-Environmental Sciences, Chinese Academy of Sciences, Beijing 100085, China
[b] University of Chinese Academy of Sciences, Beijing 100049, China
[c] School of Environmental Sciences and Engineering, Guangzhou University, Guangzhou 510006, China

ARTICLE INFO

ABSTRACT

A layered BiO(OH)$_x$I$_{1-x}$ solid solution was grown *in situ* on the surface of AgI particles by a one-pot co-crystallization method. Based on the results of XPS, EPR, XRD and other techniques, it was verified that a *p-n* heterojunction was formed through Ag-I-Bi cross-linking bonds in the interface of BiO(OH)$_x$I$_{1-x}$ and AgI due to the common species of I$^-$ ions. The resulting BiO(OH)$_x$I$_{1-x}$-AgI exhibited high efficiency and stability for photodegradation of phenolic compounds with visible light irradiation. No significant AgI decomposition or release of Ag$^+$ or Bi^{3+} was observed in the photoreaction, and the photoactivity of AgI was enhanced almost 9-fold. These enhanced photocatalytic properties were attributed to the strong interfacial interaction between BiO(OH)$_x$I$_{1-x}$ and AgI by the Ag-I-Bi bond junction. Due to the chemical-bond junction, the photogenerated electrons in the CB of AgI quickly transferred to the CB of BiO(OH)$_x$I$_{1-x}$ to produce O$_2^{•-}$, while the holes in the VB of BiO(OH)$_x$I$_{1-x}$ migrated to the VB of AgI to oxidize pollutants in water. The accelerated interfacial charge transfers were responsible for the high photostability and photoactivity of BiO(OH)$_x$I$_{1-x}$-AgI.

© 2017 Elsevier B.V. All rights reserved.

1. Introduction

Photocatalysis is a promising technology to address the issues of the energy crisis and environmental pollution that have gained considerable interdisciplinary attention [1–3]. In order to utilize the inexhaustible and clean solar energy, appropriate semiconductors are required to carry out numerous catalytic reactions [4]. In recent years, a number of photocatalytic systems such as TiO$_2$, ZnO, CdS, g-C$_3$N$_4$ have been developed, and demonstrated that photocatalysis is a feasible technology.

Silver halides (AgX, X = Cl, Br, I), well-known photosensitive materials, have been intensively studied in the fields of photocatalytic hydrogen evolution and photodegradation of organic pollutants due to their prominent photoactivity. However, they are unavoidably decomposed into metallic Ag under visible-light irradiation. In illuminated AgX, the photo-generated electrons in the conduction band (CB) can be captured by surface lattice Ag$^+$ ions

to form metallic Ag$_n$ clusters, whereas the photo-generated holes oxidize lattice X$^-$ to release X$_2$ [5]. Moreover, Ag^0 would also be photo-corroded to Ag$^+$ ions released to the water solution, causing secondary pollution during the reaction [6,7].

It has been proposed that the CB electrons of AgX can be quickly captured by another electron acceptor before reducing the lattice Ag$^+$, which may not only improve the stability, but also enhance the photocatalytic efficiency. Several previous studies, such as those on Fe(III)/AgBr [5], GN−AgBr [8], and AgI/TiO$_2$ [9], have been devoted to accelerating the migration of photo-generated electrons from AgX.

Constructing a heterojunction is an effective stratregy to enhance carrier transfer between semiconductors. When the heterojunctions are well-designed, the paths of carrier migration may even be regulated [10] to meet various needs in many works. More and more works have demonstrated semiconductor/AgX heterojunction structures exhibiting high photocatalytic efficiency, for example AgBr-BiOBr, Ag/AgBr/TiO$_2$ and Ag$_3$PO$_4$/AgI [11–13]. An efficient heterojunction requires matched band structures and tight contact between the two semiconducting materials, which can promote the smooth migration of electrons and holes in the interface [14,15].

* Corresponding author at: Key Laboratory of Drinking Water Science and Technology, Research Center for Eco-Environmental Sciences, Chinese Academy of Sciences, Beijing, 100085, China.
E-mail address: huchun@rcees.ac.cn (C. Hu).

In recent years, materials possessing a laminated structure, such as graphene [16], g-C$_3$N$_4$ [17] and MoS$_2$ [18], have aroused much attention due to their excellent physico-chemical properties. Bismuth-based materials, composed of alternating layers of [Bi$_2$O$_2$]$^{2+}$ and inorganic groups, could efficiently separate photogenerated electron-hole pairs by internal static electric fields [19]. Using various inorganic anion ions, such as Br$^-$, I$^-$, CO$_3$$^{2-}$, OH$^-$ etc. [20–22], it is easy to generate solid solutions of these [Bi$_2$O$_2$]$^{2+}$-based laminar materials. Several Bi-based solid solution photocatalysts were reported to exhibit excellent and composition-dependent performance, such as BiOCl$_{1-x}$Br$_x$ [23], BiOBr$_x$I$_{1-x}$ [24], BiO(ClBr)$_{(1-x)/2}$I$_x$ [25], BiO$_x$Cl$_y$ and BiO$_x$Br$_y$ [26]. Thus, these materials are candidates for the construction of heterojunctions that could meet various requirements under different conditions.

In this work, the BiO(OH)$_x$I$_{1-x}$ solid solution was grown *in situ* on AgI particles by a one-pot co-crystallization method to produce a chemical-bond junction between the two phases. The AgI remained undecomposed throughout the whole photocatalysis reaction, and its photocatalytic activity for the degradation and mineralization of the tested phenolic compounds was greatly enhanced under visible irradiation, as it was combined with the BiO(OH)$_x$I$_{1-x}$ solid solution by chemical bonds. A preliminary effort to identify the correlation between the structural characteristics and photocatalytic performance has been undertaken.

2. Experimental

2.1. Chemicals and materials

The reagent 5-tert-butoxycarbonyl 5-methyl-1-pyrroline N-oxide (BMPO) used as the spin trapping agent in the electron paramagnetic resonance (EPR) studies was purchased from the Bioanalytical Lab (Sarasota, FL). 2-chlorophenol (2-CP), 2, 4-dichlorophenol (2, 4-DCP), trichlorophenol (TCP), phenol, AgNO$_3$, Bi(NO$_3$)$_3$·5H$_2$O, *p*-Benzoquinone (*p*-BQ), Triethanolamine (TEOA) and all other chemicals were of analytical grade and purchased from the Beijing Chemical Company, and used without further purification.

2.2. Preparation of catalysts

The BiO(OH)$_x$I$_{1-x}$-AgI composites were synthesized through a chemical co-precipitation method. In a typical process, 0.21 g of AgNO$_3$ in 2.3 mL of NH$_4$OH (25 wt% NH$_3$) was added to 200 mL ultrapure water. Then, 8.66 mL of a 0.2 M KI solution was added dropwise to the above solution, and subsequently, 0.24 g of Bi(NO$_3$)$_3$·5H$_2$O in 10 mL of a 60 vol% acetic solution was added dropwise to the suspension and stirred at room temperature for 12 h. The generated precipitate was collected and washed several times with water to neutral conditions, and finally dried at 70 °C in air. BiO(OH)$_x$I$_{1-x}$, and AgI samples were also synthesized under identical conditions but with AgNO$_3$ or Bi(NO$_3$)$_3$·5H$_2$O absent in the synthesis process, respectively. The x value in BiO(OH)$_x$I$_{1-x}$-AgI and BiO(OH)$_x$I$_{1-x}$ samples were equal about 0.65 determined by the atomic ratio data from energy spectrum (EDS) results. And the content of BiO(OH)$_x$I$_{1-x}$ in the composite BiO(OH)$_x$I$_{1-x}$-AgI were measured as 33.8 wt% using ICP-MS (inductively coupled plasma mass spectrometer) mothed when dissolved in H$_2$SO$_4$ solution.

As a reference, BiO(OH)$_x$I$_{1-x}$ was loaded on AgI (BiO(OH)$_x$I$_{1-x}$/AgI) by a two-step method: 0.29 g of the as-prepared AgI was suspended in 200 mL ultrapure water, and 2.3 mL of NH$_4$OH and 2.46 mL of a 0.2 M KI solution was added subsequently. Then, 0.24 g of Bi(NO$_3$)$_3$·5H$_2$O in 10 mL of a 60 vol% acetic solution was added dropwise to the suspension and stirred at room temperature for 12 h. The generated precipitate

was collected and washed several times with water to neutral conditions, and finally dried at 70 °C in air.

2.3. Characterization

Powder X-ray diffraction (XRD) patterns were recorded on a Scintag-XDS-2000 diffractometer with Cu Kα radiation (λ = 1.540598 Å) operating at 40 kV and 40 mA. The morphological observations were performed by a field emission scanning electron microscope (SU 8020 FESEM; Hitachi). EDS results were obtained from a Hitachi S-3000N system. High-resolution transmission electron microscopy (HR-TEM) images were recorded using a JEOL-2010 TEM with an acceleration voltage of 200 kV. The electron paramagnetic resonance (EPR) of the solid powder samples and BMPO-O$_2$$^{•-}$, BMPO-$^•$OH in solution were obtained using a Bruker model A300-10/12 electron paramagnetic resonance spectrometer. X-ray photoelectron spectroscopy (XPS) data were obtained using an AXIS-Ultra instrument from Kratos using monochromatic Al Kα radiation and low-energy electron-flooding for charge compensation. All binding energies were calibrated by the C 1 s hydrocarbon peak at 284.80 eV. UV–vis diffuse reflectance spectroscopy (DRS, Hitachi UH4150) was also used to characterize the prepared samples. The photocurrent and Mott-Schottky analysis was performed using a basic electrochemical system (AMETEK Princeton Applied Research, Oak Ridge, TN) with a two-compartment, three-electrode electrochemical cell equipped with a photocatalyst photoanode (prepared by dip-coating and drying in air at 70 °C) and a platinum wire cathode in a 0.1 M Na$_2$SO$_4$ solution.

2.4. Photocatalytic degradation of pollutants under visible light irradiation

Photocatalytic experiments were performed in a beaker with aqueous suspensions of phenolic compounds (60 mL, 10 mg L^{-1}) containing 100 mg of catalyst powders, respectively. A 150-W Xe-arc lamp (Shanghai Photoelectron Device Ltd.) equipped with a wavelength cutoff filter to pass λ > 400 nm was used as the light source. The concentration of each chlorophenol was measured using high-performance liquid chromatography (1200 series; Agilent) with an Eclipse XDB-C18 column (5 μm, 4.6 × 150 mm; Agilent). The released Ag$^+$ concentration during photoreaction was determined by an inductively coupled plasma mass spectrometer (ICP-MS, VG Plasma Quad 3). The total organic carbon (TOC) of each solution was measured with a TOC analyzer (TOC-VCPH, Shimadzu). The by-products of 2-CP photodegradation were detected using a Dionex ICS-2000 ion chromatography system with AS-DV auto-sampler. In trapping experiments, 3 vol% triethanolamine (TEOA), 1 mM *p*-benzoquinone (*p*-BQ), 5 mM K$_2$S$_2$O$_8$, 1 mM NaN$_3$ and 100 mM *t*-butanol were added to the reaction suspensions as active species scavengers, respectively. In the recycling experiment, the photocatalyst was filtered and washed (the unwashed catalyst was also used after a statement) with ultrapure water prior to being resuspended in the 2-CP solution for another cycle.

3. Result and discussion

3.1. Characterization of photocatalysts

Fig. 1 shows the XRD patterns of BiO(OH)$_x$I$_{1-x}$, BiO(OH)$_x$I$_{1-x}$-AgI and AgI. The XRD pattern of BiO(OH)$_x$I$_{1-x}$ (Fig. 1a) is coincident with that of BiO$_m$I$_n$ reported in the literature [27]. According to the synthetic process and literature reports [26], BiO$_m$I$_n$ was formed by ion exchange of OH$^-$ with I$^-$ in [Bi$_2$O$_2$]$^{2+}$ layers, which could be best described as BiO(OH)$_x$I$_{1-x}$, indicating its structural relationship to other [Bi$_2$O$_2$]-based layered compounds. [Bi$_2$O$_2$]-(OH)$_2$·2H$_2$O (BHO) [28] and BiOI were also prepared under otherwise identical
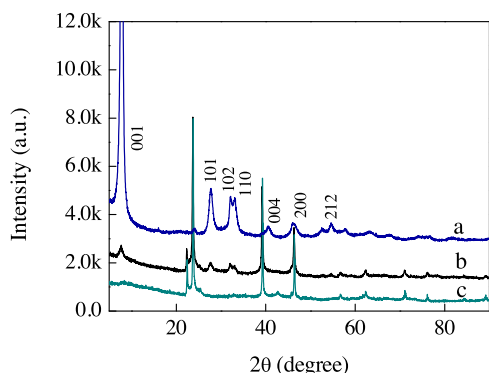
Fig. 1. The XRD patterns of $BiO(OH)_xI_{1-x}$ (a), $BiO(OH)_xI_{1-x}$-AgI (b), and AgI (c).

conditions. In BHO, $BiO(OH)_xI_{1-x}$ and BiOI (JCPDS, card nos. 10-0445) (Fig. S1), the (001) peaks shifted continuously toward BiOI from BHO, indicating that $BiO(OH)_xI_{1-x}$ was a solid solution of BiOI and BHO. Moreover, a gradually increased visible light absorption was observed in UV–vis diffuse reflectance spectra, with absorption edges at 365 nm, 558 nm and 687 nm for BHO, $BiO(OH)_xI_{1-x}$ and BiOI samples (Fig. S2), and the powder colors were white, yellow and red, which also confirmed the formation of a solid solution [24,25]. In $BiO(OH)_xI_{1-x}$-AgI (Fig. 1b), the characteristic XRD peaks of $BiO(OH)_xI_{1-x}$ appeared, but the intensity of the dominant (001) peak was much decreased in comparison with its other peaks. The result indicated that the (001) face was mainly exposed in $BiO(OH)_xI_{1-x}$; however, different crystal growth directions of $BiO(OH)_xI_{1-x}$ occurred in the heterojunction material, so that (110) and other faces of $BiO(OH)_xI_{1-x}$ had more opportunity to be exposed in $BiO(OH)_xI_{1-x}$-AgI [29,30]. The XRD peaks of AgI attributed to β-AgI were also found in $BiO(OH)_xI_{1-x}$-AgI, without other impurity phases.

In the SEM images, AgI particles were smooth and spherical with average diameter of about 1 μm (Fig. 2A), $BiO(OH)_xI_{1-x}$ formed nanometer-sized platelets in Fig. 2B, whereas the particles of $BiO(OH)_xI_{1-x}$-AgI (Fig. 2C) were below 200 nm, and $BiO(OH)_xI_{1-x}$ platelets were found to be tightly grown on AgI particles, with the platelet size about 60 nm, resulting in more active faces of $BiO(OH)_xI_{1-x}$ being exposed.

The HR-TEM images of the $BiO(OH)_xI_{1-x}$ sample demonstrated a layer structure (Fig. 3A). The distances between adjacent lattice fringes of $BiO(OH)_xI_{1-x}$ were measured as 0.32 nm (Fig. 3B). In the HR-TEM image of $BiO(OH)_xI_{1-x}$-AgI (Fig. 3C), AgI particles were found to be surrounded by $BiO(OH)_xI_{1-x}$ platelets with tight contact, and the lattice fringes of both AgI and $BiO(OH)_xI_{1-x}$ were observed at the edge of $BiO(OH)_xI_{1-x}$-AgI particle (Fig. 3D) [31].

In Fig. 4A, both $BiO(OH)_xI_{1-x}$ and $BiO(OH)_xI_{1-x}$-AgI exhibit similar O 1 s spectra, which could be fitted into two peaks at 530.3 eV and 531.5 eV attributed to the lattice oxygen O^{2-} and surface OH^- [32]. In the AgI sample, I $3d_{3/2}$ and I $3d_{5/2}$ peaks were observed at 631.5 eV and 620.1 eV, while in $BiO(OH)_xI_{1-x}$, the peaks shifted to 630.7 eV, 619.3 eV; however, in $BiO(OH)_xI_{1-x}$-AgI they were located at 631.1 eV and 619.7 eV (Fig. 4B). As the I 3d peaks in $BiO(OH)_xI_{1-x}$-AgI could not be fitted into two peaks, it was concluded that the lattice I existed in only one state, which was different from the I in AgI and $BiO(OH)_xI_{1-x}$, indicating that both AgI and $BiO(OH)_xI_{1-x}$ possessed identical lattice I states in the $BiO(OH)_xI_{1-x}$-AgI heterojunction. In addition, Ag $3d_{3/2}$ and Ag $3d_{5/2}$ peaks ascribed to Ag^+ at 374.8 eV and 368.8 eV for AgI shifted to lower binding energy at 374.5 eV and 368.5 eV for $BiO(OH)_xI_{1-x}$-AgI (Fig. 4C). Meanwhile, a small shift (+0.1 eV) was also observed for Bi $4f_{5/2}$ and $4f_{7/2}$ peaks ascribed to Bi^{3+} in $BiO(OH)_xI_{1-x}$-AgI compared with $BiO(OH)_xI_{1-x}$

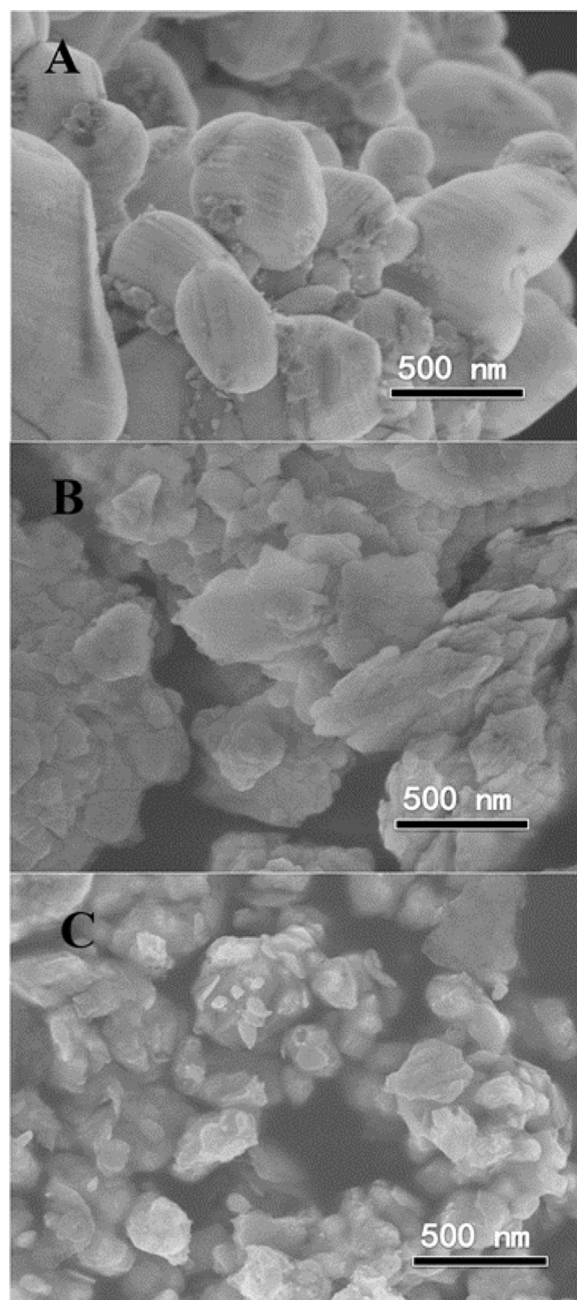**Fig. 2.** SEM images of AgI (A,), $BiO(OH)_xI_{1-x}$ (B), and $BiO(OH)_xI_{1-x}$-AgI (C).

(Fig. 4D). These results indicated that a Ag-I-Bi cross-linking bond was formed between $BiO(OH)_xI_{1-x}$ and AgI in $BiO(OH)_xI_{1-x}$-AgI [33].

In the electron paramagnetic resonance (EPR) measurements, the AgI sample obtained the highest EPR signal, with the g value (about 1.98) indicating an electron-excess center (Ag^0) on the surface of AgI [34] in Fig. 5. In contrast, the EPR signal was greatly decreased with the coating by $BiO(OH)_xI_{1-x}$ sheets, indicating that the surface electrons of AgI were stabilized. The above results indicated that an electronic spin-orbit interaction occurred between AgI and $BiO(OH)_xI_{1-x}$, verifying Ag-I-Bi chemical bond formation in $BiO(OH)_xI_{1-x}$-AgI.

The light absorption of prepared samples was measured by UV–vis DRS (Fig. 6). All the samples exhibited good absorbance in the UV and visible light range. The absorption edges of AgI, $BiO(OH)_xI_{1-x}$-AgI and $BiO(OH)_xI_{1-x}$ were around 460 nm, 550 nm and 560 nm, indicating that all of the catalysts could be excited by
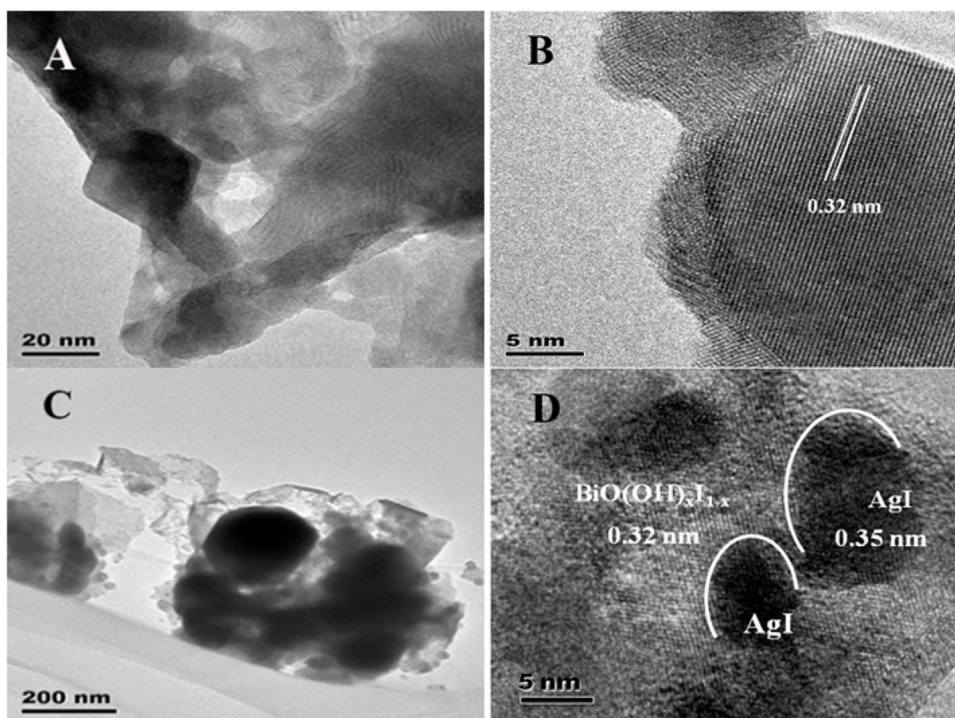
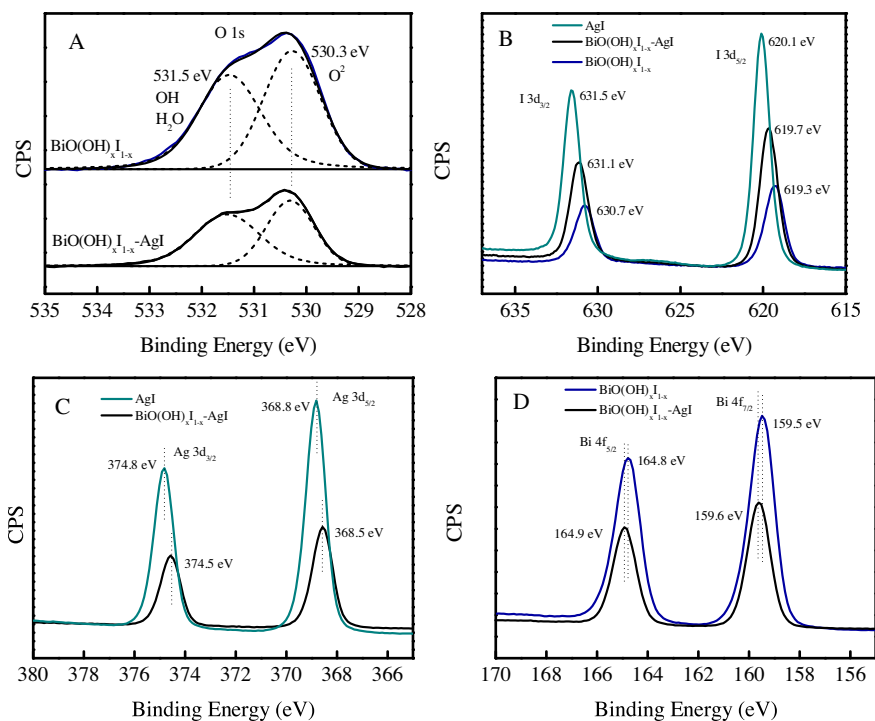**Fig. 3.** HR-TEM images of $BiO(OH)_xI_{1-x}$ (A, B), and $BiO(OH)_xI_{1-x}$-AgI (C, D).

Fig. 4. O 1s (A), I 3d (B), Ag 3d (C), Bi 4f (D) XPS high-resolution spectra obtained from AgI, $BiO(OH)_xI_{1-x}$, and $BiO(OH)_xI_{1-x}$-AgI samples.

visible light. In the photographs, the three samples all appear as yellow powdered materials, also demonstrating their good visible light harvesting ability.

3.2. Performance of photocatalysts

The performance of different photocatalysts was examined by degradation 2-CP in water. $BiO(OH)_xI_{1-x}$-AgI displayed the high-

est catalytic activity, with 10 mg/L 2-CP being completely degraded within 30 min under visible light ($\lambda > 400$ nm) irradiation (Fig. 7A). Under the same conditions, 71% of 2-CP was photodegraded in $BiO(OH)_xI_{1-x}$ suspensions, and 64% for $BiO(OH)_xI_{1-x}$/AgI, 42% for AgI. The $BiO(OH)_xI_{1-x}$/AgI sample, where $BiO(OH)_xI_{1-x}$ was supported on AgI by a two-step method, exhibited much lower reactivity than $BiO(OH)_xI_{1-x}$-AgI. The curves of $\ln(C/C_0)$ as a function of irradiation time are shown in Fig. S3, and the calculated
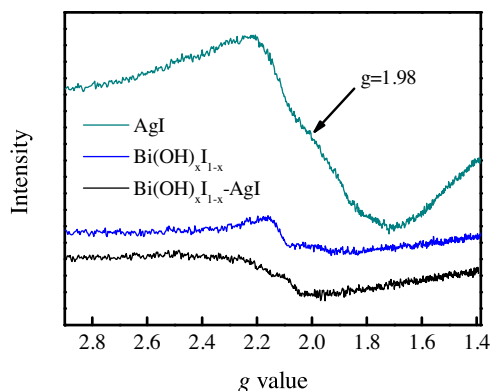
Fig. 5. EPR spectra of AgI, BiO(OH)$_x$I$_{1-x}$, and BiO(OH)$_x$I$_{1-x}$-AgI samples.

known, AgI would be decomposed under light irradiation, leading an increase in the Ag$^+$ concentration along with the photocatalytic reaction. The result indicated that AgI decomposition could be inhibited in the heterojunction BiO(OH)$_x$I$_{1-x}$-AgI suspension under visible-light irradiation, to avoid secondary pollution due to Ag$^+$ release.

In addition, 2,4,6-TCP and 2, 4-DCP were completely degraded within 20 and 30 min, respectively, and more than 70% of phenol was removed in 60 min in the BiO(OH)$_x$I$_{1-x}$-AgI suspension (Fig. 7C). Moreover, 71%, 67%, 53%, 40% of TOC was removed within 4 h for phenol, 2-CP, 2,4-DCP, and 2,4,6-TCP, respectively (Fig. 7D). The photodegradation production of 2-CP were detected after the 1 h reaction in BiO(OH)$_x$I$_{1-x}$-AgI suspension by IC mothed. Besides Cl$^-$, oxalic acid, malonic acid, fumaric acid et al. by-product were found. These small molecule acid products were recognized as non-toxic organics and more biodegradable than 2-CP.

3.3. Photostability of BiO(OH)$_x$I$_{1-x}$-AgI

The durability of BiO(OH)$_x$I$_{1-x}$-AgI, BiO(OH)$_x$I$_{1-x}$ and AgI for the degradation of 2-CP was evaluated under visible light irradiation. After ten successive cycles, the photocatalytic activity of BiO(OH)$_x$I$_{1-x}$-AgI only displayed a slight decrease from 100% to 86% (Fig. 8A). The surface active sites occupied by the adsorbed by-products and physical deterioration contributed to activity continuously reducing of BiO(OH)$_x$I$_{1-x}$-AgI photocatalyst. That was inevitable in most catalytic reaction. The photostability of BiO(OH)$_x$I$_{1-x}$ was also excellent and only 6% catalytic activity lost after ten successive cycles (Fig. 8B). In contrast, the degradation percentage of 2-CP decreased dramatically from 43% at the first cycle to 25% at the tenth cycle in the AgI suspension, indicating its photo-instability (Fig. 8C).
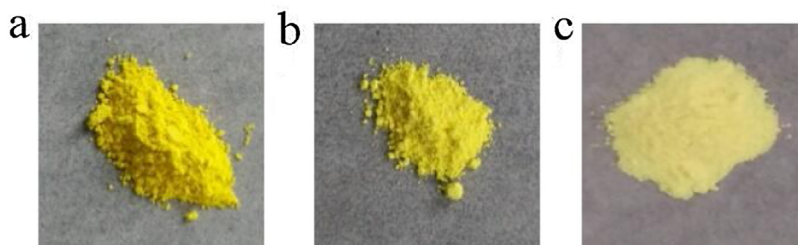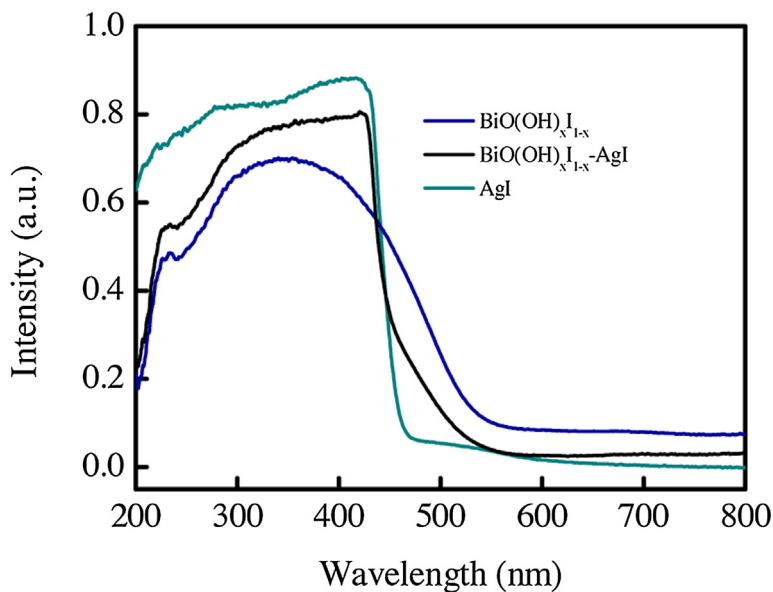
degradation rate constants are also provided. The rate constant of 2-CP degradation in the BiO(OH)$_x$I$_{1-x}$-AgI suspension was much higher than that for BiO(OH)$_x$I$_{1-x}$, BiO(OH)$_x$I$_{1-x}$/AgI, and AgI; it showed almost 9 times the degradation rate of AgI. These results demonstrated that the photocatalytic activity of BiO(OH)$_x$I$_{1-x}$ and AgI were greatly enhanced by heterojunction BiO(OH)$_x$I$_{1-x}$-AgI with electron orbital conjugation of the lattice I$^-$, verifying that the existence of a junction with Ag-I-Bi bonds between individual semiconductors favored their interfacial electron transfer.

Ag$^+$ ions released in different catalyst suspensions were simultaneously detected during photoreaction (Fig. 7B). In the AgI suspension, the Ag$^+$ concentration was 165 μg/L after a 30 min dark equilibration reaction, then increased to 253 μg/L after the photoreaction. Surprisingly, no Ag$^+$ was detected in the BiO(OH)$_x$I$_{1-x}$-AgI suspension before or after irradiation. As is

Fig. 6. UV–vis diffuse reflectance spectra of different samples and the photographic images of BiO(OH)$_x$I$_{1-x}$ (a), BiO(OH)$_x$I$_{1-x}$-AgI (b), and AgI (c).
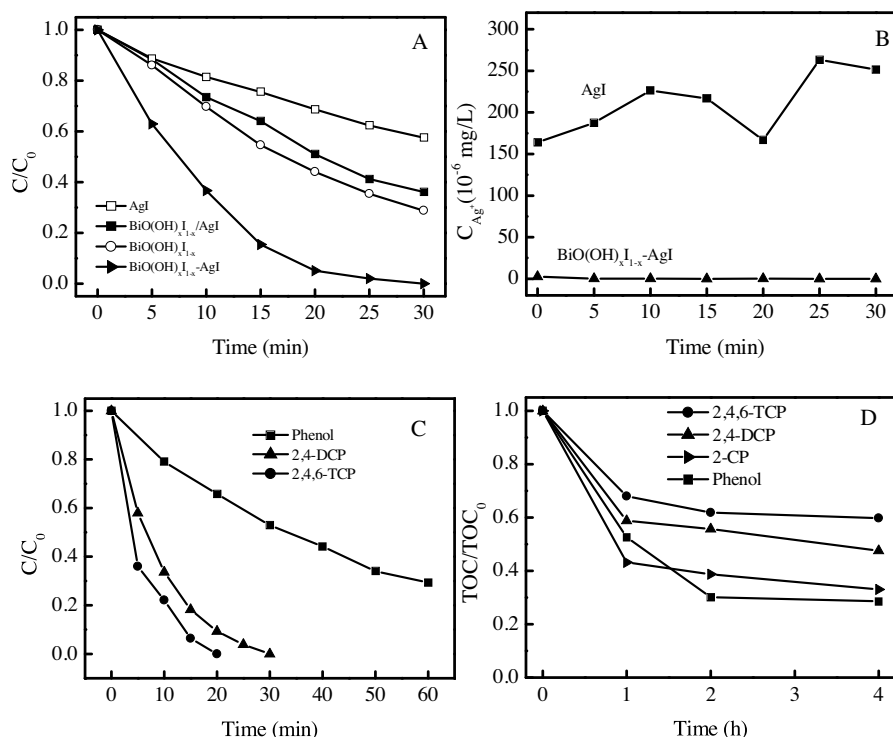
Fig. 7. Temporal course of 2-CP photodegradation in different photocatalyst suspensions (A) and the corresponding Ag^+ released in the reaction solutions (B); temporal course of phenolic compound photodegradation (C) and the corresponding TOC removal curves (D).

In order to simulate the real application, the cycling run experiments were conducted without washing the $BiO(OH)_xI_{1-x}$-AgI photocatalyst after filtrated from solution (Fig. 9). In the 2nd degradation experiment, about 6% photoactivity lost. But after five successive cycles, the photocatalytic activity of $BiO(OH)_xI_{1-x}$-AgI only decreased 12%, that was almost similar with the washing result (10%) in Fig. 8A.

UV-vis DSR curves were also recorded during the cycling-run degradation experiment. For $BiO(OH)_xI_{1-x}$-AgI, after the 5th or 10th reactions, the curves almost coincided with the curve obtained from the fresh sample (Fig. 10A). However, for AgI, an obvious absorption band appeared around 550 nm after the 5th and 10th reactions, as shown in Fig. 10B, which was assigned to the surface plasmon absorption of Ag NPs [3]. The phenomenon verified Ag^0 formation during AgI photocatlysis, indicating the photo-decomposition of AgI. In addition, $BiO(OH)_xI_{1-x}$/AgI also showed an absorption band above 500 nm after visible light irradiation, indicating that AgI was also photo-decomposed in the material without a chemical-bond junction (Fig. 10C). The results indicated that Ag-I-Bi chemical-bond junction enhanced the interfacial electron transfer, thus inhibiting the decomposition of AgI in $BiO(OH)_xI_{1-x}$-AgI.

3.4. Reaction mechanism and band gap structure

The effects of different active-species scavengers on the photodegradation of 2-CP were examined in $BiO(OH)_xI_{1-x}$-AgI suspensions with visible light ($\lambda > 400$ nm) irradiation (Fig. 11). With the addition of *p*-BQ as $O_2^{\bullet-}$ scavenger or TEOA as h^+ scavenger, 2-CP degradation were greatly suppressed. When $K_2S_2O_8$, as e^- scavenger, or a N_2 atmosphere were used in the reaction, the photodegradation of 2-CP also obviously decreased. As active electrons in the CB could react with dissolved oxygen molecules to generate $O_2^{\bullet-}$ radical, it was deduced that $O_2^{\bullet-}$ and h^+ were the main active species in the photodegradation experiment. h^+ scavenger (TEOA) and N_2 purging were simultaneously used to evaluate the contri-

bution of electrons in phenolic compound degradation, and 2-CP degradation was much depressed. As the result was similar with the only addition of TEOA, there was no clear evidence that electrons could degrade 2-CP directly. The CB electrons mainly play a role in the photoreaction through generating $O_2^{\bullet-}$ with O_2 molecule. On the contrary, the photocatalytic degradation of 2-CP was not affected by the addition of NaN_3 (a quencher of $\cdot O_2{}^1$) and *t*-Butanol (a quencher of $\bullet OH$), thus $O_2{}^1$ and $\bullet OH$ did not play important roles in the degradation of 2-CP. As expected, in the EPR measurement with BMPO, the signals of BMPO-$O_2^{\bullet-}$ were observed in a methanol dispersion of $BiO(OH)_xI_{1-x}$-AgI under visible light irradiation, but no obvious signals of BMPO-$\bullet OH$ were found in the aqueous dispersion (Fig. 12). These results demonstrated that $O_2^{\bullet-}$ radical generated from conduction band (CB) electrons contributed to organic degradation, meanwhile valence band (VB) holes could also oxidize organics directly in visible-irradiated $BiO(OH)_xI_{1-x}$-AgI suspensions.

The transient photocurrent response of ITO/photocatalyst electrodes could examine the e^--h^+ separation efficiency, which is known to be a decisive factor influencing the photocatalytic reaction. In Fig. 13, about $+15\,\mu A$, $-14\,\mu A$, $-15\,\mu A$ and $-52\,\mu A$ were observed for AgI, $BiO(OH)_xI_{1-x}$/AgI, $BiO(OH)_xI_{1-x}$ and $BiO(OH)_xI_{1-x}$-AgI photoanodes respectively. The largest separation and transfer efficiency of photo-generated e^--h^+ pairs were achieved with $BiO(OH)_xI_{1-x}$-AgI, which was attributed to the chemical-bond junction between $BiO(OH)_xI_{1-x}$ and AgI.

For a crystalline semiconductor, it has been shown that the optical absorption near the band edge follows the equation [24]:

$$\alpha h\nu = A(h\nu - E_g)^{n/2}$$

where α, ν, E_g, and A are the absorption coefficient, the light frequency, the bandgap, and a constant, respectively. The factor n decides the characteristics of the transition in a semiconductor, and the value of n is 1 or 4 for a direct or indirect bandgap material, respectively. As an indirect bandgap semiconductor [35], the
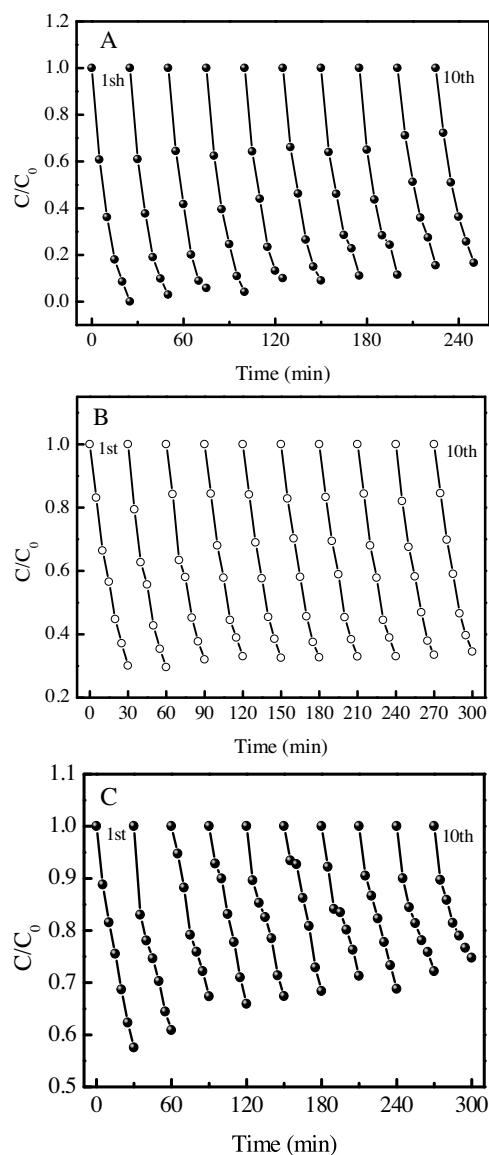
Fig. 8. Successive runs in the photodegradation of 2-CP under visible light irradiation in $BiO(OH)_xI_{1-x}$-AgI (A), $BiO(OH)_xI_{1-x}$ (B) or AgI (C) suspensions.
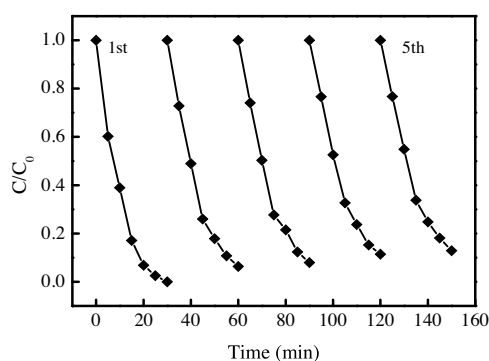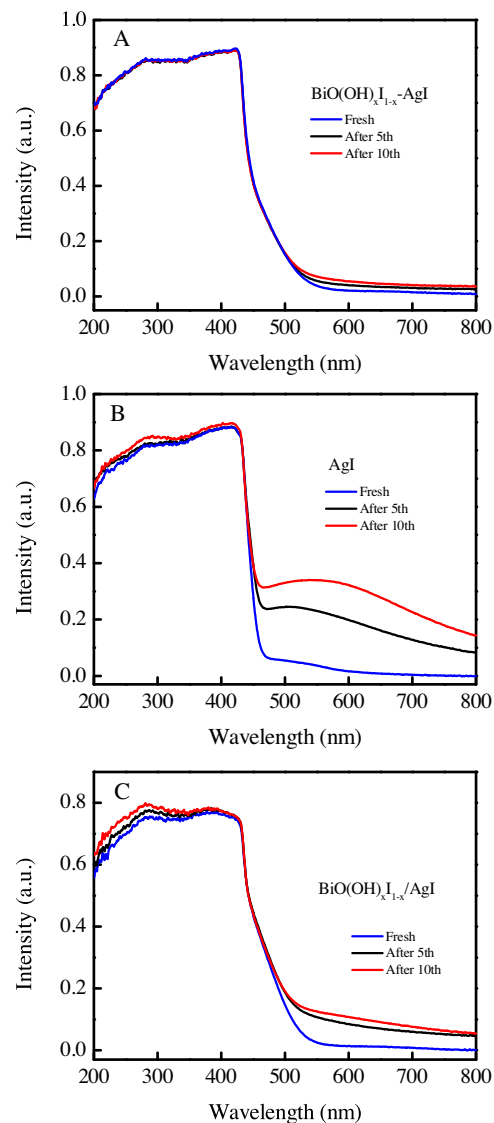

Fig. 10. UV–vis diffuse reflectance spectra in successive runs of photodegradation experiments of $BiO(OH)_xI_{1-x}$-AgI (A), AgI (B) and $BiO(OH)_xI_{1-x}$/AgI (C).

Fig. 9. Successive runs in the photodegradation of 2-CP under visible light irradiation in $BiO(OH)_xI_{1-x}$-AgI suspensions without washing the photocatalyst after each run.
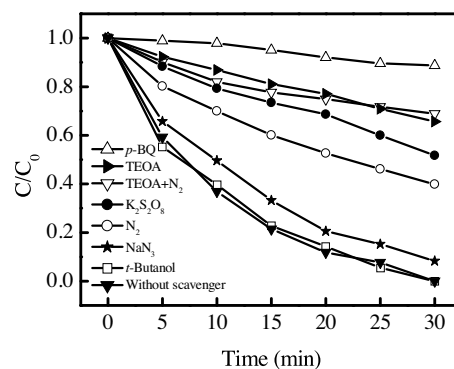

Fig. 11. Temporal course of the 2-CP photodegradation in $BiO(OH)_xI_{1-x}$-AgI suspension with the addition of different radical scavengers.
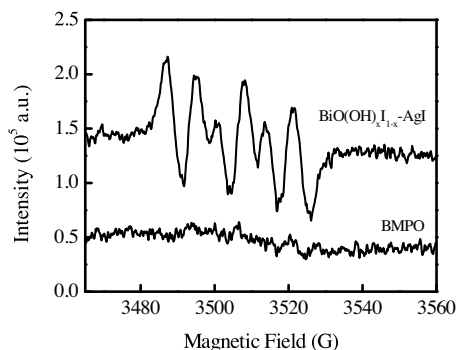
Fig. 12. BMPO spin-trapping EPR spectra in methanol dispersion for BMPO—$O_2^{\bullet-}$.

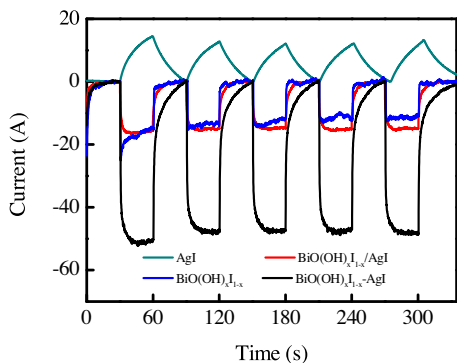**Fig. 13.** The transient photocurrent response of different electrodes.

Fig. 15. The band gap structure of BiO(OH)$_x$I$_{1-x}$-AgI *p-n* heterojunction photocatalyst.

bandgap of BiO(OH)$_x$I$_{1-x}$ was calculated from the UV–vis DSR result in Fig. 6 and given in Fig. 14A as 2.40 eV. The electronic energy band characteristics of BiO(OH)$_x$I$_{1-x}$ were examined by electrochemical impedance spectroscopic analysis along with the Mott-Schottky equation [36,37], that is

$$\frac{1}{C^2} = \frac{2}{e\varepsilon\varepsilon_0 N_A}\left(E - E_F - \frac{kT}{e}\right)$$

where C represents the capacitance of the space-charge region, ε_0 is the vacuum permittivity, ε is the dielectric constant of the BiO(OH)$_x$I$_{1-x}$, e is the electron charge, E is the applied potential, k is the Boltzmann constant, T is the absolute temperature, and N_A is the acceptor density (or donor density). The temperature term is generally small and can be neglected. As shown in Fig. 14B, the slope of the linear $1/C^2$ potential curve of BiO(OH)$_x$I$_{1-x}$ is negative, indicating that the as-prepared BiO(OH)$_x$I$_{1-x}$ was a p-type semiconductor [29]. Therefore, the VB potential of BiO(OH)$_x$I$_{1-x}$ could be read as +1.84 eV *vs* $E_{Ag/AgCl}$ and calculated as +2.44 eV *vs* NHE. Thus the CB potential was calculated as +0.04 eV *vs* NHE by the equation:
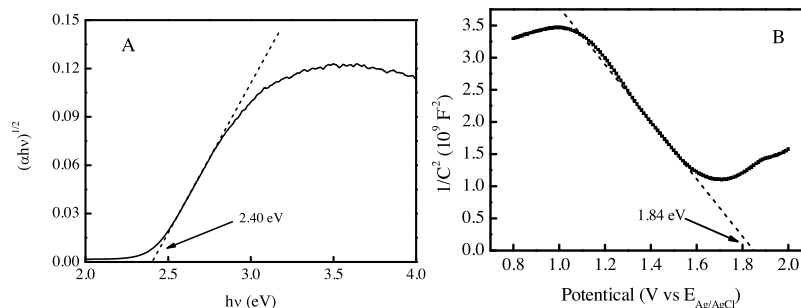
$$E_{CB} = E_{VB} - E_g$$

Silver halide materials have always been regarded as n-type semiconductors, and active electrons as the main carriers [11,38]. However, because the AgI catalyst was unstable in the experiments, the literature values E_{CB} −0.38 eV and E_{VB} +2.34 eV *vs* NHE derived from theoretical calculation were used [13].

On the basis of all the above information, the photocatalytic mechanism for BiO(OH)$_x$I$_{1-x}$-AgI was derived as illustrated in Fig. 15: BiO(OH)$_x$I$_{1-x}$ and AgI both could be excited by visible light. In the Z-scheme band system, as the CB position of AgI is more negative than that of BiO(OH)$_x$I$_{1-x}$, photogenerated electrons in the CB of AgI migrated to the CB of BiO(OH)$_x$I$_{1-x}$ via the orbital interaction of the Ag-I-Bi bond. Because the VB position of BiO(OH)$_x$I$_{1-x}$ is more positive than that of AgI, its VB holes migrated to the VB of AgI also via the orbital interaction of the Ag-I-Bi bond. Therefore, the transfer of photogenerated carriers was very favorable at the interface of BiO(OH)$_x$I$_{1-x}$ and AgI via the Ag-I-Bi bond in BiO(OH)$_x$I$_{1-x}$-AgI. Thus, the recombination of electrons and holes not only was suppressed, but also more active electrons and holes contributed to the pollutant degradation reaction. Moreover, since the photoexcited electrons of AgI were transferred to the CB of BiO(OH)$_x$I$_{1-x}$ effectively, the reaction of AgI photo-corrosion to Ag^0 was completely inhibited, improving the stability of the AgI catalyst. The electrons in the CB of BiO(OH)$_x$I$_{1-x}$ could be trapped by dissolved oxygen molecules to generate $O_2^{\bullet-}$ radical, which was a main active species for pollutant degradation. Meanwhile, the photo-generated holes in the VB of AgI, as another important active species, could oxidize organic pollutants directly in the photocatalysis reaction.

Fig. 14. (A) Plots of $(\alpha h\nu)^{1/2}$ versus photon energy ($h\nu$) for BiO(OH)$_x$I$_{1-x}$ photocatalyst. (B) Mott-Schottky diagram of a BiO(OH)$_x$I$_{1-x}$ electrode.

4. Conclusions

BiO(OH)$_x$I$_{1-x}$-AgI was synthesized by a one-pot co-crystallization method, in which the *p-n* heterojunction was formed by the junction of Ag-I-Bi bonds. The photocatalyst was demonstrated to have high activity and stability in the degradation and mineralization of 2-CP, 2,4-DCP, and TCP under visible light irradiation. The Ag-I-Bi bond junction enhanced the separation and transfer of photo-generated carriers at the interface of BiO(OH)$_x$I$_{1-x}$-AgI, almost completely inhibiting AgI photodecomposition. Furthermore, it was demonstrated that O$_2$•$^-$ radical and holes were the main active species in the photocatalytic reaction. Photostability and photocatalytic mechanisms for BiO(OH)$_x$I$_{1-x}$-AgI were proposed based on all experimental information. These findings indicated that heterojunction formation by electron orbital interaction of individual phases is crucial for high efficiency separation and transfer of photogenerated carriers.

Acknowledgements

Appendix A. Supplementary data

Supplementary data associated with this article can be found, in the online version, at http://dx.doi.org/10.1016/j.apcatb.2017.06.077.

References

[1] M.R. Hoffmann, S.T. Martin, W.Y. Choi, D.W. Bahnemann, Chem. Rev. 95 (1995) 69–96.
[2] R. Asahi, T. Morikawa, T. Ohwaki, K. Aoki, Y. Taga, Science 293 (2001) 269–271.
[3] S. Linic, P. Christopher, D.B. Ingram, Nat. Mater. 10 (2011) 911–921.
[4] W.J. Ong, L.L. Tan, Y.H. Ng, S.T. Yong, S.P. Chai, Chem. Rev. 116 (2016) 7159–7329.
[5] H. Yu, L. Xu, P. Wang, X. Wang, J. Yu, Appl. Catal. B 144 (2014) 75–82.
[6] X. Hu, X. Zhou, R. Wang, C. Hu, J. Qu, Appl. Catal. B 154–155 (2014) 44–50.
[7] C. Hu, T. Peng, X. Hu, Y. Nie, X. Zhou, J. Qu, H. He, J. Am. Chem. Soc. 132 (2010) 857–862.
[8] M.S.A. Sher Shah, W.J. Kim, J. Park, D.K. Rhee, I.H. Jang, N.G. Park, J.Y. Lee, P.J. Yoo, ACS Appl. Mater. Interfaces 6 (2014) 20819–20827.
[9] W. Sun, Y. Li, W. Shi, X. Zhao, P. Fang, J. Mater. Chem. 21 (2011) 9263–9270.
[10] H. Wang, L. Zhang, Z. Chen, J. Hu, S. Li, Z. Wang, J. Liu, X. Wang, Chem. Soc. Rev. 43 (2014) 5234–5244.
[11] L. Kong, Z. Jiang, H.H. Lai, R.J. Nicholls, T. Xiao, M.O. Jones, P.P. Edwards, J. Catal. 293 (2012) 116–125.
[12] C. Hu, Y. Lan, J. Qu, X. Hu, A. Wang, J. Phys. Chem. B 110 (2006) 4066–4072.
[13] Z. Chen, W. Wang, Z. Zhang, X. Fang, J. Phys. Chem. C 117 (2013) 19346–19352.
[14] H. Cheng, B. Huang, P. Wang, Z. Wang, Z. Lou, J. Wang, X. Qin, X. Zhang, Y. Dai, Chem. Commun. 47 (2011) 7054–7056.
[15] X. Zong, H. Yan, G. Wu, G. Ma, F. Wen, L. Wang, C. Li, J. Am. Chem. Soc. 130 (2008) 7176–7177.
[16] X. Huang, X. Qi, F. Boey, H. Zhang, Graphene-based composites, Chem. Soc. Rev. 41 (2012) 666–686.
[17] Y. Zheng, J. Liu, J. Liang, M. Jaroniec, S.Z. Qiao, Energy Environ. Sci. 5 (2012) 6717.
[18] B. Radisavljevic, A. Radenovic, J. Brivio, V. Giacometti, A. Kis, Nature nanotech. 6 (2011) 147–150.
[19] S. Meng, X. Zhang, G. Zhang, Y. Wang, H. Zhang, F. Huang, Inorg. Chem. 54 (2015) 5768–5773.
[20] F. Dong, Q. Li, Y. Sun, W.-K. Ho, ACS Catal. 4 (2014) 4341–4350.
[21] H. Cheng, B. Huang, Y. Dai, Nanoscale 6 (2014) 2009–2026.
[22] S. Shenawi-Khalil, V. Uvarov, S. Fronton, I. Popov, Y. Sasson, Appl. Catal. B 117–118 (2012) 148–155.
[23] Y. Liu, W.J. Son, J. Lu, B. Huang, Y. Dai, M.H. Whangbo, Chem. Eur. J. 17 (2011) 9342–9349.
[24] Z. Jia, F. Wang, F. Xin, B. Zhang, Ind. Eng. Chem. Res. 50 (2011) 6688–6694.
[25] G. Liu, T. Wang, S. Ouyang, L. Liu, H. Jiang, Q. Yu, T. Kako, J. Ye, J. Mater. Chem. A 3 (2015) 8123–8132.
[26] H. Deng, J. Wang, Q. Peng, X. Wang, Y. Li, Chem. Eur. J. 11 (2005) 6519–6524.
[27] Y.R. Jiang, H.P. Lin, W.H. Chung, Y.M. Dai, W.Y. Lin, C.C. Chen, J. Hazard Mater. 283 (2015) 787–805.
[28] S. Shenawi-Khalil, V. Uvarov, S. Fronton, I. Popov, Y. Sasson, J. Phys. Chem. C 116 (2012) 11004–11012.
[29] H. Huang, Y. He, X. Du, P.K. Chu, Y. Zhang, ACS Sustainable Chem. Eng. 3 (2015) 3262–3273.
[30] M. Pan, H. Zhang, G. Gao, L. Liu, W. Chen, Environ. Sci. Technol. 49 (2015) 6240–6248.
[31] H. Cheng, B. Huang, Y. Dai, X. Qin, X. Zhang, Langmuir 26 (2010) 6618–6624.
[32] Y. Huo, J. Zhang, M. Miao, Y. Jin, Appl. Catal. B 111-112 (2012) 334–341.
[33] G. Lassaletta, A. Fernandez, J.P. Espinos, A.R. Gonzalezelipe, J. Phys. Chem. 99 (1995) 1484–1490.
[34] D.B. Mohan, C.S. Sunandana, J. Phys. Chem. B 110 (2006) 4569–4575.
[35] W.L. Huang, Q. Zhu, J. Comput. Chem. 30 (2009) 183–190.
[36] T.F. Yeh, F.F. Chan, C.T. Hsieh, H. Teng, J. Phys. Chem. C 115 (2011) 22587–22597.
[37] X. Yang, A. Wolcott, G. Wang, A. Sobo, R.C. Fitzmorris, F. Qian, J.Z. Zhang, Y. Li, Nano Lett. 9 (2009) 2331–2336.
[38] J.F. Bringley, R.S. Eachus, A.P. Marchetti, J. Phys. Chem. B 106 (2002) 5346–5350.